

PREPARED FOR SUBMISSION TO JCAP

The effects of He I $\lambda 10830$ on helium abundance determinations

Erik Aver^a Keith A. Olive^{b,c,d} Evan D. Skillman^{b,d}

^aDepartment of Physics, Gonzaga University,
502 E Boone Ave, Spokane, WA 99258

^bSchool of Physics and Astronomy, University of Minnesota,
116 Church St. SE, Minneapolis, MN 55455

^cWilliam I. Fine Theoretical Physics Institute, University of Minnesota,
116 Church St. SE, Minneapolis, MN 55455

^dMinnesota Institute for Astrophysics, University of Minnesota,
116 Church St. SE, Minneapolis, MN 55455

E-mail: aver@gonzaga.edu, olive@umn.edu, skillman@astro.umn.edu

Abstract. Observations of helium and hydrogen emission lines from metal-poor extragalactic H II regions, combined with estimates of metallicity, provide an independent method for determining the primordial helium abundance, Y_p . Traditionally, the emission lines employed are in the visible wavelength range, and the number of suitable lines is limited. Furthermore, when using these lines, large systematic uncertainties in helium abundance determinations arise due to the degeneracy of physical parameters, such as temperature and density. Recently, Izotov, Thuan, & Guseva (2014) have pioneered adding the He I $\lambda 10830$ infrared emission line in helium abundance determinations. The strong electron density dependence of He I $\lambda 10830$ makes it ideal for better constraining density, potentially breaking the degeneracy with temperature. We revisit our analysis of the dataset published by Izotov, Thuan, & Stasińska (2007) and incorporate the newly available observations of He I $\lambda 10830$ by scaling them using the observed-to-theoretical Paschen-gamma ratio. The solutions are better constrained, in particular for electron density, temperature, and the neutral hydrogen fraction, improving the model fit to data, with the result that more spectra now pass screening for quality and reliability, in addition to a standard 95% confidence level cut. Furthermore, the addition of He I $\lambda 10830$ decreases the uncertainty on the helium abundance for all galaxies, with reductions in the uncertainty ranging from 10-80%. Overall, we find a reduction in the uncertainty on Y_p by over 50%. From a regression to zero metallicity, we determine $Y_p = 0.2449 \pm 0.0040$, consistent with the BBN result, $Y_p = 0.2470 \pm 0.0002$, based on the Planck determination of the baryon density. The dramatic improvement in the uncertainty from incorporating He I $\lambda 10830$ strongly supports the case for simultaneous (thus not requiring scaling) observations of visible and infrared helium emission line spectra.

Contents

1	Introduction	1
2	The diagnostic power of the infrared He emission line, $\lambda 10380$	3
3	Characterizing the impact of He I $\lambda 10380$ with synthetic testing	5
4	The ITG14 observations and dataset	8
5	Tracking the effects of He I $\lambda 10380$	9
6	Results from the Final Dataset	15
7	Discussion	16

1 Introduction

Although the determination of the fundamental parameters of the standard cosmological model including dark matter and dark energy, Λ CDM, by WMAP [1, 2] and Planck [3, 4] are unparalleled, big bang nucleosynthesis and the observations of the light element abundances offer an important cross-check, in particular on the determination of the baryon density. The most recent Planck result [4] for the baryon density, $\Omega_B h^2 = 0.02226 \pm 0.00016$, corresponds to a baryon-to-photon ratio of $\eta = (6.10 \pm 0.04) \times 10^{-10}$. Because the uncertainty in η is now less than 1%, standard big bang nucleosynthesis (SBBN) [5–7] is a parameter-free theory [8], and relatively precise predictions of the primordial abundances of the light elements D, ^3He , ^4He , and ^7Li are available [9–22]. While the ^7Li abundance remains problematic [17], recent D/H determinations from quasar absorption systems have become quite precise, in their own right, and they are in excellent agreement with the prediction from SBBN and the CMB [23]. Using a neutron mean life of 880.3 ± 1.1 s [24], SBBN yields a primordial abundance for ^4He , Y_p , of $Y_p = 0.2471 \pm 0.0002$, using the Planck determined value of η [22]. By allowing Y_p to vary as an independent parameter, fits to CMB anisotropies allow for a determination of Y_p within the context of Λ CDM. The recent Planck results found $Y_p = 0.251 \pm 0.027$ [4]. Fortunately, the helium abundance from emission line measurements provide significantly better precision.

To test SBBN beyond D/H, it is clear that precise determinations of ^4He are necessary. In addition, ^4He still provides important constraints on the physics of the early universe beyond the standard model [25]. Nevertheless, obtaining better than 1% precision for individual objects remains a challenge. ^4He abundance determinations are generally fraught with systematic uncertainties and degeneracies among the input parameters needed to model emission line fluxes [26, 27, 37]. The primordial abundance of ^4He is determined by fitting the helium abundance versus metallicity (oxygen), and extrapolating back to very low metallicity [28].

Our method for determining the ^4He abundance in an individual H II region is based on a Markov Chain Monte Carlo (MCMC) analysis [29–31]. Using calculated emissivities [32, 33], we model emission fluxes for a number of H and He lines relative to $\text{H}\beta$. The model depends on several physical parameters associated with the H II region: electron density,

n_e , temperature, T , optical depth τ , underlying stellar H and He absorption, a_H and a_{He} , reddening, $C(H\beta)$, the fraction of neutral hydrogen, ξ , and, of course, the He abundance, parametrized in terms of the abundance by number (relative to H) of ionized He, y^+ . MCMC scans of our 8-dimensional parameter space map out the likelihood function based on the χ^2 given by

$$\chi^2 = \sum_{\lambda} \frac{\left(\frac{F(\lambda)}{F(H\beta)} - \frac{F(\lambda)}{F(H\beta)_{meas}} \right)^2}{\sigma(\lambda)^2}, \quad (1.1)$$

where the emission line fluxes, $F(\lambda)$, are measured and calculated for six helium lines ($\lambda\lambda 3889, 4026, 4471, 5876, 6678, \text{ and } 7065$) and three hydrogen lines ($H\alpha, H\gamma, H\delta$), each relative to $H\beta$. The χ^2 in eq. 1.1 runs over all He and H lines and $\sigma(\lambda)$ is the measured uncertainty in the flux ratio at each wavelength.

We also adopt a weak prior on the temperature based on the temperature derived from [O III] emission lines. $\chi_T^2 = (T - T(OIII))^2 / \sigma^2$ is added to eq. 1.1, where we adopt $\sigma = 0.2 T_{meas}$, which is much greater than the estimated temperature difference of 11% between the measurements of temperature from ionized helium and doubly ionized oxygen lines [34–36]. For more detail on the applied temperature prior see Aver et al. [29, AOS2]. Here we also discuss the implications of removing the prior.

Once minimized, best-fit solutions for the eight physical parameter inputs, including y^+ , are found, and uncertainties in each quantity can be obtained by calculating a 1D marginalized likelihood. With eight parameters and only nine observables, our model is nearly under-determined.

This MCMC analysis was applied to the large HeBCD dataset of Izotov, Thuan, & Stasińska [37, ITS07] in Aver et al. [30, AOS3]. As discussed in AOS3, we consider only those objects with measured He I $\lambda 4026$ emission lines. We then select those objects with $\chi^2 < 4$, corresponding to a standard $\sim 95\%$ confidence level for one degree of freedom. Using a revised set of emissivities [32, 33], in our most recent work, Aver et al. [31, AOPS], we found only 16 objects which satisfy this criterion and could be used to extrapolate to zero metallicity and determine Y_p . Due to the large uncertainties in y^+ found for each object, and the relatively small number of objects for which the model acceptably describes the data, the uncertainty on our determination of Y_p was not much better than 4%.

Recently, Izotov, Thuan, & Guseva [38, ITG14] presented data for the near-infrared He I $\lambda 10830$ emission line for a large sample of metal-poor nebulae and pioneered the addition of this line in helium abundance analyses. While not only providing an additional test for the model, this particular line shows a strong sensitivity to the electron density. It can, therefore, be very useful in breaking the degeneracy between density and temperature [27, 39], allowing for more accurate determinations of y^+ in each region. Here, we make use of these new observations in a new MCMC analysis. We consider only observations for which all seven He lines have reported values in ITS07 & ITG14 [37, 38]. While the initial data set is reduced (not every object measured in ITS07 has a measured He I $\lambda 10830$ emission line in ITG14 and vice versa), better constrained parameters allow more objects to yield statistically reliable and physically meaningful solutions. As a result, we base our current analysis on 15 objects (with some, but not full, overlap with the sample used in AOPS [31]). The uncertainty in y^+ in individual objects is, in fact, significantly reduced (by as much as 80%) and the extrapolated primordial abundance is now determined to 1.6%: $Y_p = 0.2449 \pm 0.0040$.

This paper is organized as follows. First, §2 introduces He I $\lambda 10830$, with particular emphasis on its electron density dependence. Second, in §3, Monte Carlo testing with synthetic

data including He I $\lambda 10830$ is carried out to examine its diagnostic power. This includes examining cases both with and without the inclusion of an O[III] temperature prior. Third, §4 offers a brief overview of the ITG14 observations and dataset, along with the required scaling of the He I $\lambda 10830$ observations. In §5, the set of ITS07 galaxies in ITG14 are analyzed, demonstrating the impact of He I $\lambda 10830$ on the solutions. Subsequently, Y_p is determined in §6. Finally, §7 offers a discussion of the results, possible systematic effects or additional uncertainties, and the benefits of further observations with He I $\lambda 10830$.

2 The diagnostic power of the infrared He emission line, $\lambda 10380$

He I $\lambda 10830$ is emitted in a 2^3P to 2^3S transition ($\Delta\ell = 1$). Corresponding to its small energy change ($\Delta E = 1.14$ eV), it is readily collisionally excited from the metastable 2^3S triplet state. It is this large population due to collisional excitation that makes it so sensitive to the H II region’s density. Figure 1 shows the sensitivity to density for all of the He emission lines considered. The figure clearly shows the dramatically stronger density dependence of He I $\lambda 10830$, with a slope over four times greater than that of the next most sensitive line, He I $\lambda 7065$. Therefore, we expect that He I $\lambda 10830$ should be an excellent density diagnostic, greatly constraining the density in our solutions. Figure 2 shows the temperature dependence of the He emission lines considered. He I $\lambda 10830$ does not stand out, as it did in figure 1, but its temperature dependence is the second strongest, and, furthermore, its increase with temperature helps to balance out the three strong optical lines, He I $\lambda\lambda 4471, 5876, \& 6678$, all of whose emissivities decrease similarly with temperature.

The He line flux ratios (compared to H β) used in eq. (1.1) are calculated using

$$\frac{F(\lambda)}{F(H\beta)} = y^+ \frac{E(\lambda)}{E(H\beta)} \frac{\frac{W(H\beta)+a_H(H\beta)}{W(H\beta)}}{\frac{W(\lambda)+a_{He}(\lambda)}{W(\lambda)}} f_\tau(\lambda) \frac{1}{1 + \frac{C}{R}(H\beta)} 10^{-f(\lambda)C(H\beta)}, \quad (2.1)$$

where $W(\lambda)$ is the measured equivalent width, and two parameters, a_H and a_{He} , characterize the wavelength-dependent underlying absorption for H and He, respectively. The function $f_\tau(\lambda)$ represents a correction for radiative transfer and depends on τ , n_e , and T . The emissivity, E , including the He collisional corrections, is a function of n_e , and T . The hydrogen collisional corrections are accounted for by $\frac{C}{R}$, which depends on the fraction of neutral-to-ionized hydrogen, ξ . The final term in eq. (2.1) accounts for reddening, $C(H\beta)$. See AOS & AOS2 [29, 39] for full details on the model and analysis method.

To incorporate He I $\lambda 10830$ into our analysis, the following data are used. The emissivities, including the collisional correction, are adopted from the recent work of Porter, Ferland, Storey, & Detisch [33], as was implemented in AOPS [31], and include He I $\lambda 10830$. The radiative transfer equations in terms of optical depth come from the work of Benjamin, Skillman, & Smits [40]. That work does not include a fitting formula for He I $\lambda 10830$, however. Instead, the 10-level numerical calculation program was graciously provided by Bob Benjamin (private communication). Fitting the same functional form to the He I $\lambda 10830$ optical depth data over the same range ($n_e = 1\text{-}300$ cm $^{-3}$ and $T = 1.2\text{-}2.0 \times 10^4$ K), we obtain:

$$f_\tau(10830) = 1 + (\tau/2)[0.0149 + (4.45 \times 10^{-3} - 6.34 \times 10^{-5}n_e + 9.20 \times 10^{-8}n_e^2)T], \quad (2.2)$$

with a maximum fit error of 1.3% (similar to the maximum fit errors reported in [40]). Correcting for the effects of underlying absorption for He I $\lambda 10830$ is more tenuous since the

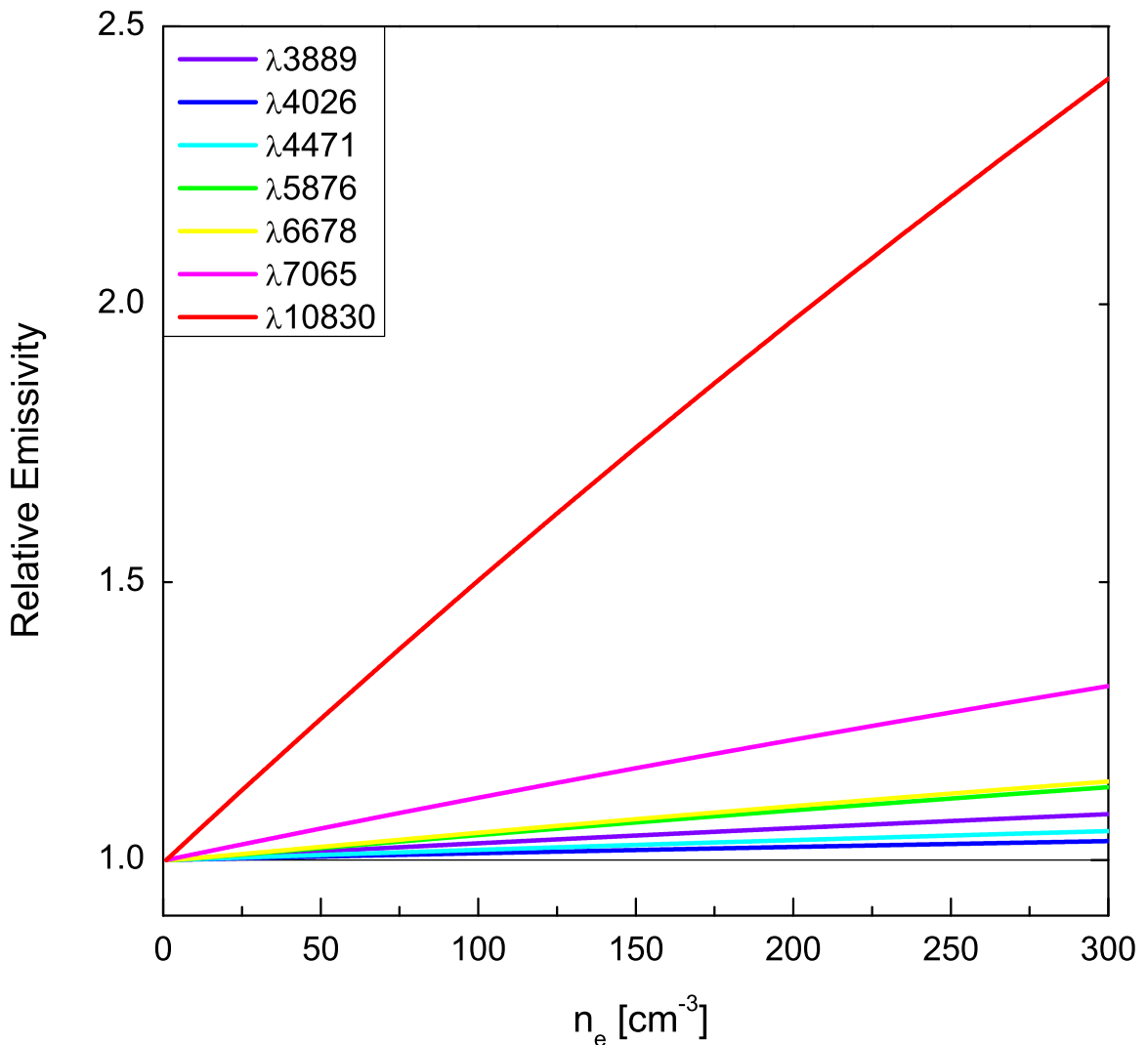


Figure 1. Comparison of the Porter, Ferland, Storey, & Detisch [33] emissivities, including the collisional correction, versus density, using a temperature of 18,000 K, for He I $\lambda\lambda 3889, 4026, 4471, 5876, 6678, 7065, 10830$. The much stronger density dependence of He I $\lambda 10830$ is apparent.

available data is very limited. The 3 B-star supergiant spectra (where helium absorption is more significant) reported in Conti & Howarth [41] show equivalent width (EW) underlying absorption of $\sim 0.5\text{-}2.0$ Å. Because the EW of He I $\lambda 10830$ is large (typically 100-400 Å), the correction of underlying absorption will be reassuringly small. For this work, we adopt an underlying absorption coefficient of 0.8, relative to He I $\lambda 4471$ (i.e., He I $\lambda 4471$ carries a coefficient of 1.0), such that the underlying absorption correction applied will be $0.8 \times a_{He}$, where a_{He} is the solution for underlying absorption (see AOS for further details [39]). This ratio of 0.8 for underlying absorption of He I $\lambda 10830$ relative to that of He I $\lambda 4471$ is the same as in adopted by ITG14 [38] (though the approaches to determining the underlying absorption differ).

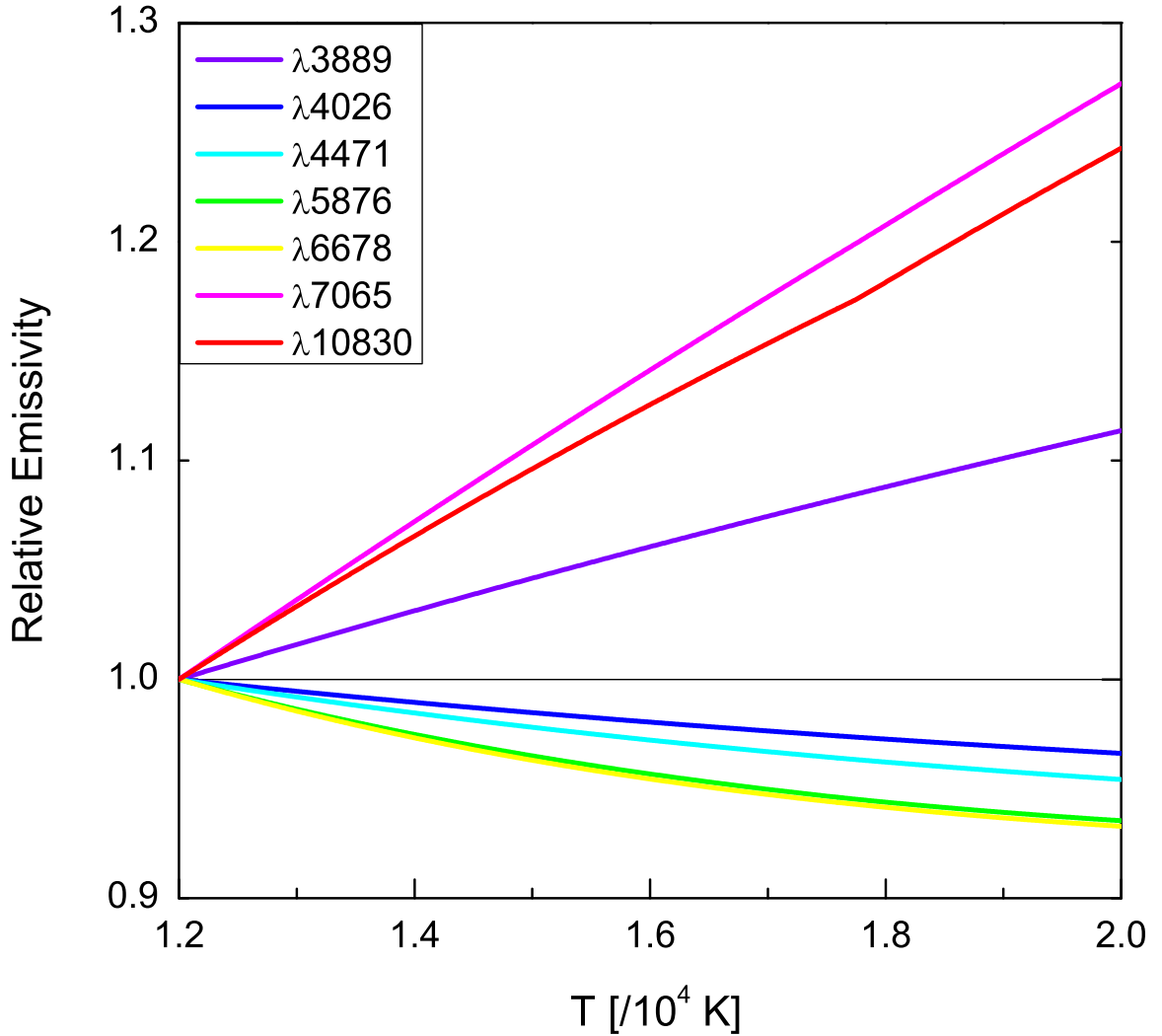


Figure 2. Comparison of the Porter, Ferland, Storey, & Detisch [33] emissivities, including the collisional correction, versus temperature, using a density of 100 cm^{-3} , for He I $\lambda\lambda 3889, 4026, 4471, 5876, 6678, 7065, 10830$.

3 Characterizing the impact of He I $\lambda 10380$ with synthetic testing

To begin discerning the effect and potential benefits of He I $\lambda 10380$, we conduct Monte Carlo analyses using synthetic data, since it offers a controlled environment for clear comparisons. First, a set of input parameters were used to generate a synthetic spectrum. These are given in the second column of table 1. Then, 1000 sets of Gaussian perturbed fluxes were calculated with spreads of 3% and 1.5% of the unperturbed helium and hydrogen fluxes, respectively. The best-fit solution (via χ^2 minimization, see AOS [39]) of each of these 1000 perturbed spectra was then found. Finally, the average value and dispersion of those 1000 solutions was calculated for each parameter. To allow comparisons showing the effects of He I $\lambda 10380$ and the [O III] temperature prior, this process was repeated for the following four cases: analysis with He I $\lambda 10380$ & with T(O III) included, without He I $\lambda 10380$ but with T(O III), with He I $\lambda 10380$ but without T(O III), and without He I $\lambda 10380$ & without T(O III). The results

of these MC simulations for y^+ vs. both n_e and T (the electron density and temperature solved for from the helium and hydrogen emission lines) are shown in figure 3. The average value and dispersion for each of the four cases is provided in table 1.

	Input	w/ T(O III) & w/ He I λ 10830	w/ T(O III)	w/ He I λ 10830	w/o T(O III) & w/o He I λ 10830
y^+	0.085	0.0858 ± 0.0027	0.0857 ± 0.0063	0.0860 ± 0.0028	0.0867 ± 0.0071
n_e	500.0	473 ± 67	555 ± 402	460 ± 174	2570^{+6980}_{-2570}
a_{He}	0.5	0.52 ± 0.11	0.51 ± 0.15	0.51 ± 0.12	0.53 ± 0.14
τ	1.0	0.78 ± 0.31	0.80 ± 0.73	0.62 ± 0.56	0.52 ± 0.72
T_e	16,000	$17,320 \pm 1090$	$17,400 \pm 1300$	$18,860 \pm 4190$	$18,300 \pm 5320$
C(H β)	0.1	0.09 ± 0.03	0.09 ± 0.03	0.09 ± 0.03	0.08 ± 0.04
a_H	1.0	2.08 ± 1.47	2.10 ± 1.70	2.61 ± 2.09	2.69 ± 2.15
$\xi \times 10^4$	1.0	13^{+19}_{-13}	14^{+31}_{-14}	$1040^{+31,620}_{-1040}$	8570^{+68530}_{-8570}
T(O III)	17,000				

Table 1. Comparison of MC distributions with synthetic data

When the [O III] prior and He I λ 10830 are included, the input data are nicely reproduced. As the figure and table clearly show, He I λ 10830 dramatically reduces the uncertainty on the density (by over 75%), as well as improving the average, both with and without the inclusion of the T(O III) prior. As a result of the degeneracy between temperature and density (see OS04 & AOS [27, 39]), the uncertainty on the temperature is also decreased. Corresponding to the better constrained density and temperature, the precision on the helium abundance, y^+ , is greatly increased. The inclusion of He I λ 10830 decreases the uncertainty on y^+ by over 50%, when either the T(O III) prior is or is not included. In fact, in terms of the uncertainty on y^+ , the inclusion of He I λ 10830 mostly obviates the benefit of the T(O III) prior. However, the T(O III) prior still has a large effect in improving the temperature determination.

The neutral hydrogen fraction, ξ , is very poorly constrained for very low temperatures, due to its exponential temperature dependence (see AOS [39]). As a result, the T(O III) prior's exclusion of the lowest temperatures is crucial in restraining the range of MC solutions for ξ . Objects with completely unphysical best-fit solutions for ξ (i.e., >25% neutral hydrogen) are excluded (see AOS3 [30]). Therefore, the T(O III) prior still offers potential utility in our analysis here, even if it does not improve the determination of y^+ when He I λ 10830 is included. It should be noted that we first implemented T(O III) as a weak prior to rule out unphysical double minima in some solutions (see AOS2 [29]). The much better constrained density in the presence of He I λ 10830 has a similar effect, thus allowing for the possibility of removing the non-parametric prior.

As can be seen particularly in the lowest of the density panels in figure 3, some MC realizations have solutions for which the density increases to very large values. This is a consequence of the temperature-density degeneracy, and as discussed above, the corresponding very low temperatures allow the neutral hydrogen fraction to increase almost without bound (see AOS for further discussion [39]). To see the extent of the range in density found in this case, we provide an inset in that figure. As a result of the extended range in n_e , the MC average values are biased upward for n_e and ξ , with a correspondingly large uncertainty, as can be seen in the inset and the last column of table 1. This is one of the drawbacks of Monte

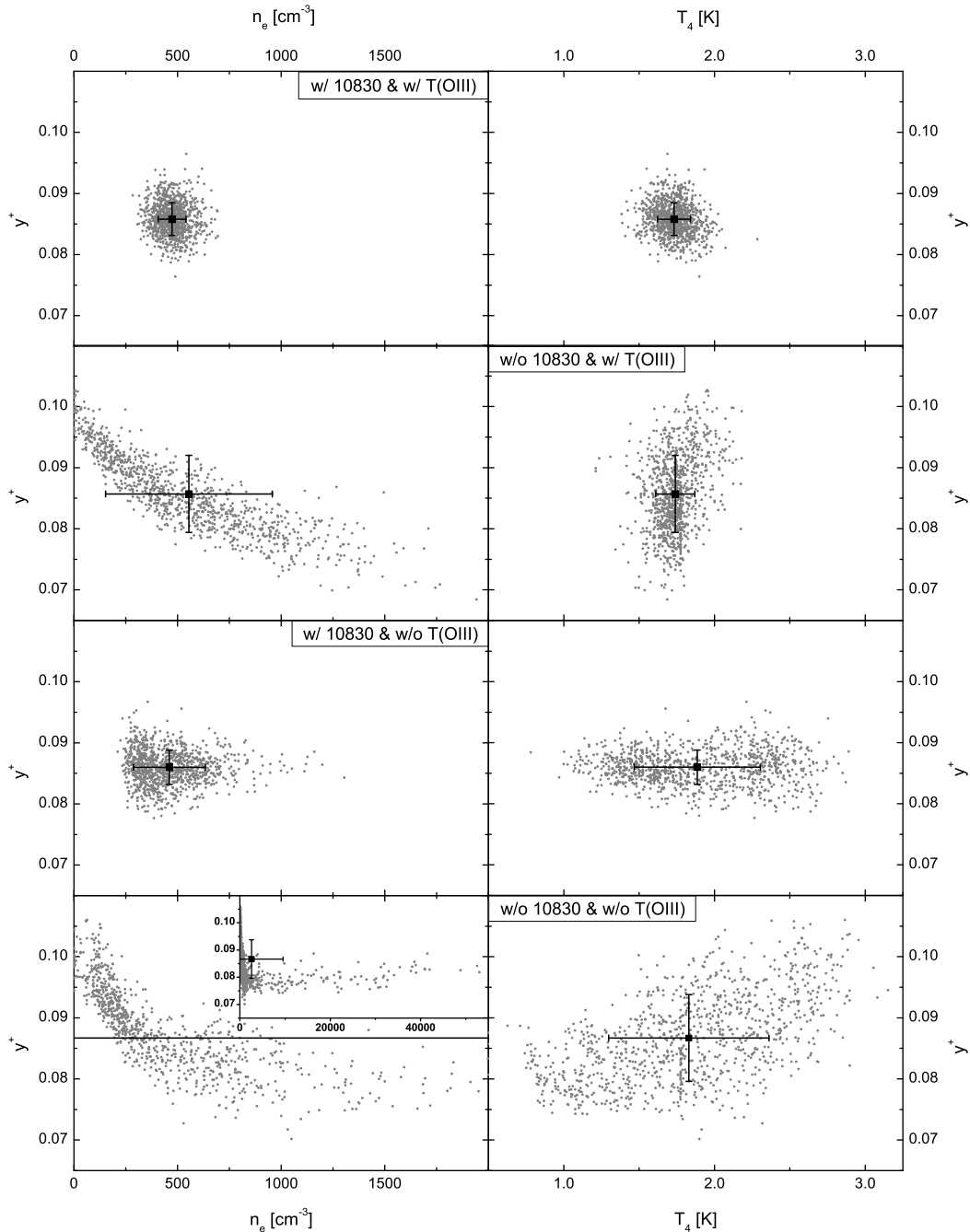


Figure 3. Comparison of 1000 MC solutions for analysis with and without He I $\lambda 10830$, as well as with and without the [O III] temperature prior. For each of these four cases, the helium abundance is plotted separately versus density and temperature. On each of these eight panels the average MC best-fit value is plotted with its dispersion. From top to bottom the progression of the panels is as labeled: w/ He I $\lambda 10830$ & w/ T(O III), w/o He I $\lambda 10830$ & w/ T(O III), w/ He I $\lambda 10830$ & w/o T(O III), and w/o He I $\lambda 10830$ & w/o T(O III). The panels on the left are y^+ vs. n_e , while those on the right are y^+ vs. T , and, except for the inset in the bottom left panel, all of the axes are shared and show the same domain and range.

Carlo via flux perturbation, as was discussed in AOS [39]. The MCMC method introduced in AOS2 [29] is not sensitive to this same behavior. Nevertheless, the distribution of perturbed solutions is very effective at illustrating the effects of the T(O III) prior and of He I λ 10830.

For a further demonstration of the effects of He I λ 10830, one of the flux perturbed synthetic spectra was analyzed using the MCMC analysis we employ to determine the solutions to the physical parameter set [29–31]. Rather than examining the distribution of 1000 flux simulations, the spectrum, synthetic or otherwise, is treated as an observation, for which a Monte Carlo over the eight model parameters (y^+ , n_e , a_{He} , τ , T, C(H β), a_H , ξ) is performed to determine the uncertainties about the best-fit values. For one of the flux perturbed synthetic spectra, the solution (with uncertainties) was found for the same four cases discussed above and is reported in table 2. The conclusions from the above analysis are reinforced, with He I λ 10830 tremendously improving the density determination, both the best-fit value and the uncertainty. This, in turn, improves the helium abundance determination. Comparing the solutions with and without He I λ 10830, the 68% confidence level uncertainty range for the density is decreased by $\sim 75\%$ & $\sim 80\%$, for the cases with and without the T(O III) prior, respectively, while the uncertainty in y^+ sees corresponding decreases of $\sim 40\%$ & $\sim 50\%$. Again, the efficacy of He I λ 10830 in improving our solutions is impressive.

	Input	w/ T(O III) &		w/o T(O III) &	
		w/ He I λ 10830	w/ T(O III)	w/ He I λ 10830	w/o He I λ 10830
y^+	0.085	0.0870 $^{+0.0036}_{-0.0017}$	0.0805 $^{+0.0056}_{-0.0031}$	0.0872 $^{+0.0037}_{-0.0015}$	0.0815 $^{+0.0062}_{-0.0040}$
n_e	500.0	457 $^{+135}_{-117}$	995 $^{+681}_{-469}$	519 $^{+226}_{-250}$	747 $^{+2540}_{-355}$
a_{He}	0.5	0.48 $^{+0.12}_{-0.08}$	0.38 $^{+0.13}_{-0.10}$	0.50 $^{+0.10}_{-0.09}$	0.38 $^{+0.14}_{-0.10}$
τ	1.0	1.42 $^{+0.38}_{-0.68}$	0.00 $^{+0.61}_{-0.00}$	1.60 $^{+0.38}_{-1.02}$	0.00 $^{+0.62}_{-0.00}$
T_e	16,000	15,400 $^{+4222}_{-2052}$	17,620 $^{+2310}_{-2870}$	14,210 $^{+6880}_{-2310}$	19,380 $^{+2520}_{-8980}$
C(H β)	0.1	0.13 $^{+0.02}_{-0.04}$	0.08 $^{+0.03}_{-0.03}$	0.12 $^{+0.02}_{-0.03}$	0.08 $^{+0.03}_{-0.04}$
a_H	1.0	0.10 $^{+3.07}_{-0.10}$	3.89 $^{+1.68}_{-2.11}$	0.00 $^{+3.13}_{-0.00}$	4.20 $^{+1.52}_{-3.91}$
$\xi \times 10^4$	1.0	0 $^{+112}_{-0}$	26 $^{+136}_{-26}$	0 $^{+370}_{-0}$	12 $^{+1024}_{-12}$
χ^2		3.11	1.47	2.71	1.37
T(O III)	17,000				

Table 2. Comparison of MCMC solutions with synthetic data

4 The ITG14 observations and dataset

Izotov, Thuan, & Guseva [38, ITG14] have recently published their observations of helium abundances using He I λ 10830. The ITG14 dataset consists of near-infrared measurements of He I λ 10830 and hydrogen emission line Paschen γ λ 10940 Å (P γ) from 45 H II regions in 43 low metallicity galaxies. The majority of the observations, 33 of 45, were made with the 3.5 m Apache Point Observatory and TripleSpec spectrograph; 8 observations were taken with the 8.4 m Large Binocular Telescope and Lucifer spectrograph, as it allows observations of fainter, often lower metallicity, galaxies; and finally, four observations were retrieved from the European South Observatory data archives (2 VLT & 2 NTT). ITG14 combine these near-infrared spectra with 75 optical spectra taken from those 43 galaxies, where some galaxies have multiple independent observations. Because the near-infrared and optical spectra were

taken with different telescopes, apertures, and at different times, the measured He I $\lambda 10830$ flux must be scaled to match the optical flux measurements. Similar to ITG14 [38], we scale He I $\lambda 10830$ using the observed $P\gamma$ flux and the theoretical flux ratio for $P\gamma$ relative to $H\beta$.

$$\begin{aligned} \frac{F(\lambda 10830)}{F(H\beta)} &= \frac{F(\lambda 10830)}{F(P\gamma)} \frac{F(P\gamma)}{F(H\beta)} \\ \frac{F(\lambda 10830)}{F(H\beta)} &= \frac{F(\lambda 10830)}{F(P\gamma)} \frac{E(P\gamma)}{E(H\beta)} \frac{\frac{W(H\beta)+a_H(H\beta)}{W(H\beta)}}{\frac{W(P\gamma)+a_H(P\gamma)}{W(P\gamma)}} \frac{1 + \frac{C}{R}(P\gamma)}{1 + \frac{C}{R}(H\beta)} 10^{-f(P\gamma)C(H\beta)}. \end{aligned} \quad (4.1)$$

The theoretical flux ratio for $P\gamma$ relative to $H\beta$ is calculated analogously to eq. (2.1). As for all of the hydrogen emission lines, the emissivity ratio for $P\gamma$ relative to $H\beta$ is taken from Hummer & Storey [42]. The collisional correction for $P\gamma$ is calculated, as in AOS [39], using collisional excitation rates from Anderson et al. [43] (similar to $H\delta$) and recombination rates from Hummer & Storey [42]. The estimate of the underlying absorption correction for $P\gamma$ is potentially much more significant than for He I $\lambda 10830$ because it is an intrinsically weaker emission line and is constrained by the same lack of data as in the case of He I $\lambda 10830$. The same 3 B-star supergiants discussed in §2 show a similar ~ 0.5 - 2.0 Å EW of underlying absorption for $P\gamma$ [41]. For this work, we adopt an underlying absorption coefficient of 0.4, relative to $H\beta$ (i.e., $H\beta$ carries a coefficient of 1.0), such that the underlying absorption correction applied will be $0.4 \times a_H$, where a_H is the solution for underlying absorption based on all of the hydrogen lines (see AOS for further details [39]).

Of the 45 H II regions with measured He I $\lambda 10830$ emission lines reported in ITG14 [38], 26 are also present in the 93 observations comprising the HeBCD dataset of ITS07 [37], which we have previously analyzed in AOS3 & AOPS [30, 31]. Of the 93 HeBCD objects, He I $\lambda 4026$ is detected for 70. To reduce systematic uncertainty that may be introduced by the absence of He I $\lambda 4026$ (see AOS3 for further details [30]), objects where He I $\lambda 4026$ is not reported are excluded in our analysis. Of the 26 H II regions in the HeBCD for which He I $\lambda 10830$ is reported in ITG14, He I $\lambda 4026$ is detected for 22. However, of those 22, several have multiple independent observations, increasing the total number of spectra with both He I $\lambda 10830$ and He I $\lambda 4026$ to 31. Those 31 sets of observations, with optical spectra taken from ITS07 and near-infrared from ITG14, comprise our initial dataset for this work.

5 Tracking the effects of He I $\lambda 10830$

For the 31 HeBCD observations from ITS07 [37] with He I $\lambda 10830$ observations reported in ITG14 [38], the effects of including He I $\lambda 10830$ into our helium abundance analysis is examined for two cases. First, we examine the effects of the addition of He I $\lambda 10830$ to the analysis of AOPS [31]. As discussed earlier, in AOS2, AOS3, & AOPS [29–31], a temperature prior based on [O III] emission lines was utilized to eliminate unphysical double minima and improve the parameter determination. However, it is a non-parametric (i.e., not fully “self-consistent”) portion of our model, and it introduces a small bias in the solution. Due the inclusion of He I $\lambda 10830$, the T(O III) prior is no longer needed to eliminate double minima, and synthetic testing in §3 showed that its benefit in reducing parameter uncertainties was greatly reduced by the inclusion of He I $\lambda 10830$. Therefore, we also examine the effects of removing the T(O III) prior once He I $\lambda 10830$ is included.

For each of these analyses, cuts on the dataset are made following AOS3 [30] (also employed in AOPS [31]). Of primary interest is the standard 95% confidence level cut. In AOS3, there was one degree of freedom (9 fluxes relative to $H\beta$ and 8 model parameters). However, with the addition of He I $\lambda 10830$, there are now two degrees of freedom in our analysis. Therefore, a 95% confidence level corresponds to $\chi^2 < 6$, and best-fit solutions with $\chi^2 > 6$ were excluded. Furthermore, objects with unphysical physical parameters, specifically $\xi > 0.333$ (>25% neutral hydrogen), were also excluded. Of the remaining, qualifying objects, objects with large corrections for systematic effects were flagged to limit potential systematic errors introduced by uncertainties in the models. Objects with $\tau > 4$ and $\xi > 0.01$, where the $1-\sigma$ lower bound does not encompass $\xi = 0.001$, were flagged.

In the analysis of AOPS [31], the 31 objects in our present dataset broke down as follows: 11 qualifying, 2 flagged (for $\tau > 4$), and 18 excluded, 12 for $\chi^2 > 4$, 3 for $\xi > 0.333$, and 3 for both. When He I $\lambda 10830$ is added, the 11 previously qualifying objects are retained as qualifying. One of the flagged objects is now qualifying, the other is still flagged for τ . Six previously excluded objects are no longer excluded, four qualifying and two flagged (for ξ). Thus, the number of qualifying objects increases from 11 to 16, while the total number of flagged objects increases by one (from 2 to 3). If the T(O III) prior is then removed, only three originally excluded objects are reclaimed, one qualifying, and two flagged (for ξ), and one originally flagged object is excluded (the other remains flagged for τ). As a result, the qualifying and flagged datasets each increase by only one, from 11 to 12 and 2 to 3, respectively. As a final note on qualifying and flagged objects, two of the qualifying and one of the flagged observations in the analysis retaining the T(O III) prior, SBS 0335-052E1, SBS 0335-052E3, & SBS 0335-052E3, respectively, are independent observations of the same H II region. As such, they are combined by weighted average into a single object, reducing the number of qualifying objects from 16 to 15, and the distinct flagged objects from 3 to 2.

For the 11 jointly qualifying objects in AOPS and this work, figures 4 & 5 compare the best-fit solutions and uncertainties for y^+ , n_e , and T_4 ($T_e/10^4$), first for the addition of He I $\lambda 10830$, and then for the removal of the T(O III) prior. In figure 4, the effect of including He I $\lambda 10830$ is examined. The AOPS values (whose analysis utilized the T(O III) prior) are plotted adjacent to the results where He I $\lambda 10830$ is included (and the T(O III) prior is retained). The uncertainties for y^+ show decreases ranging from 10-80% (see upper panel). As was seen in §3, this substantial improvement in the determination of y^+ stems from the dramatically better constrained density. The 68% confidence level density range is reduced by over 60%, with most objects seeing their uncertainty range on the density decrease by around 85% (see middle panel). Due to the temperature-density degeneracy (see OS04 & AOS [27, 39]), the better constrained density results in a reduced temperature uncertainty (see lower panel). As density and temperature are the most important parameters in relating the helium abundance to the observed flux, y^+ is correspondingly better determined. Note that in all cases, the new solutions are fully consistent with the prior solutions, though now with greatly reduced uncertainties. The best-fit values for y^+ decrease overall (4 of 11 increase, 7 decrease), but the average reduction in the helium abundance is small, approximately 2%.

Figure 5 shows the same parameter comparisons but examines the effect of removing T(O III) prior after He I $\lambda 10830$ has been added. Therefore, both series include He I $\lambda 10830$, and the results without and with the T(O III) are plotted adjacent to each other. Overall, there is a slight improvement in the parameter determinations from the inclusion of the T(O III) prior, but it is not nearly as dramatic as in figure 4. The uncertainties on y^+ generally decrease by 5-10% due to the inclusion of the T(O III) prior (see figure 5, upper

panel).

Because the addition of He I $\lambda 10830$ increases the constraint on the density so strongly, the T(O III) prior is no longer needed to eliminate unphysical double minima, while the T(O III) prior's benefit in determining y^+ is greatly reduced (as was shown in §3 and figure 5). However, as discussed in §3, the neutral hydrogen fraction, ξ , is very poorly constrained for low temperatures, due to its exponential temperature dependence (see AOS [39]). As a result, the T(O III) prior combined with He I $\lambda 10830$ helps to constrain the temperatures further than either does individually. The preclusion of the lowest temperatures restricts ξ and prevents the solution being excluded due to a completely unphysical best-fit value for ξ ($>25\%$ neutral hydrogen). Therefore, because the T(O III) prior allows three more objects to qualify, increasing the qualifying dataset by 25% compared to adding He I $\lambda 10830$ but removing the T(O III) prior, we favor retaining the T(O III) prior for this analysis.

This dataset of 15 qualifying objects and 2 flagged objects (analyzed including both He I $\lambda 10830$ & the T(O III) prior) comprises our Final Dataset. These are the objects for which the model is a good fit and which returns physically meaningful parameter solutions. As discussed above and as shown in figure 4, the parameter determinations of their solutions are significantly improved compared to our analysis in AOPS [31], which did not include He I $\lambda 10830$. The best-fit solutions and uncertainties of the Final Dataset are presented in table 3, and they are used to determine Y_p in the following section (§6).

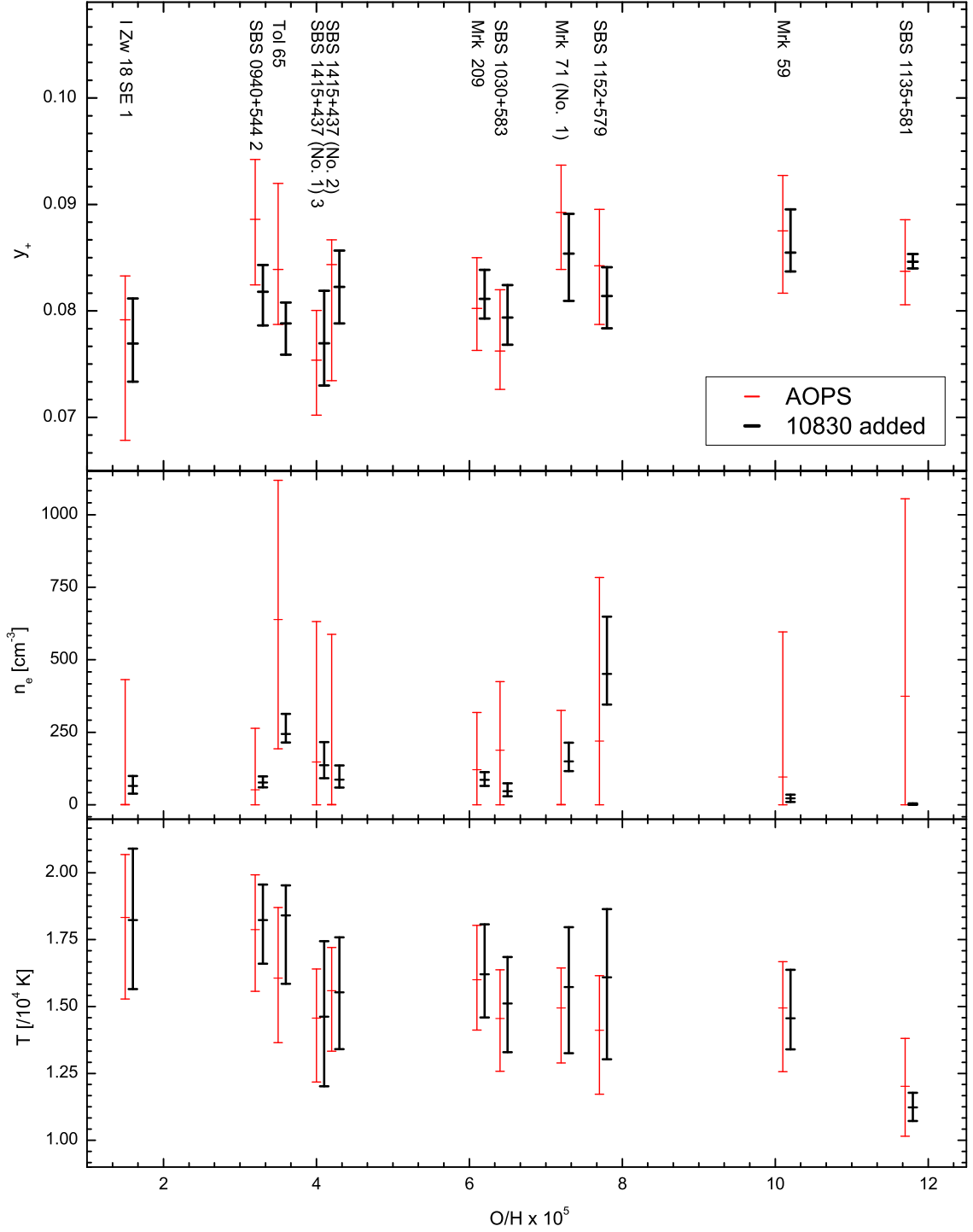


Figure 4. Plot comparing the parameter solutions for y^+ , n_e , and T_4 ($T_e/10^4$) for the 11 qualifying objects in AOPS with He I $\lambda 10830$ values in ITG14. The lighter, thinner lines show the results given in AOPS. The results after the inclusion of He I $\lambda 10830$ are given in the darker, thicker bars. The uncertainty in n_e is dramatically reduced by the addition of He I $\lambda 10830$ with a corresponding reduction in the uncertainty in y^+ .

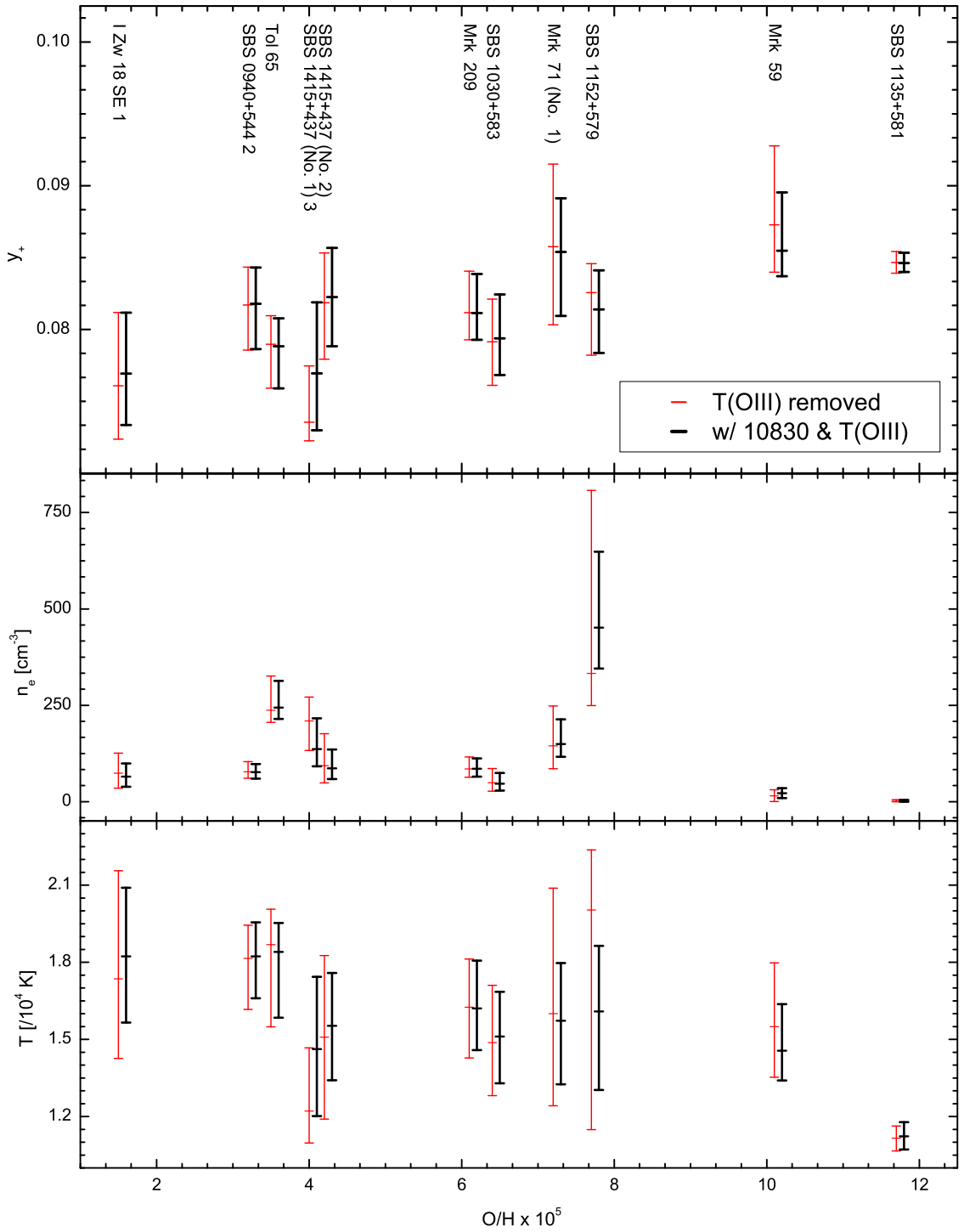


Figure 5. Plot comparing the parameter solutions for y^+ , n_e , and T_4 ($T_e/10^4$) for the 11 qualifying objects in AOPS with He I $\lambda 10830$ values in ITG14. The lighter, thinner lines show the results where He I $\lambda 10830$ is included but the T(O III) prior is removed. The results including both He I $\lambda 10830$ and the T(O III) prior are given in the darker, thicker bars. Because including the T(O III) prior does not significantly bias the values of y^+ , and because its inclusion results in a greater yield of qualifying points, the T(O III) prior is applied in the final analysis.

Object	He ⁺ /H ⁺	n _e	a _{He}	τ	T _e	C(Hβ)	a _H	ξ × 10 ⁴	χ ²
Final Dataset Not Flagged (Qualifying)									
I Zw 18 SE 1	0.07693 ^{+0.00423} _{-0.00358}	65 ⁺³⁴ ₋₂₆	0.19 ^{+0.21} _{-0.19}	0.31 ^{+0.71} _{-0.31}	18,227. ^{+2670.} _{-2575.}	0.01 ^{+0.02} _{-0.01}	3.96 ^{+0.84} _{-0.74}	1 ⁺¹³ ₋₁	0.4
SBS 0335-052E1	0.07859 ^{+0.00418} _{-0.00470}	154 ⁺⁷² ₋₃₈	0.08 ^{+0.14} _{-0.08}	3.97 ^{+0.92} _{-0.68}	20,669. ^{+2213.} _{-3920.}	0.09 ^{+0.02} _{-0.03}	3.33 ^{+1.44} _{-1.65}	6 ⁺³⁵ ₋₆	0.8
SBS 0335-052E3	0.08443 ^{+0.00396} _{-0.00385}	138 ⁺⁵³ ₋₂₈	0.32 ^{+0.08} _{-0.08}	2.39 ^{+0.74} _{-0.67}	21,780. ^{+3316.} _{-3807.}	0.21 ^{+0.02} _{-0.02}	0.98 ^{+1.10} _{-0.98}	7 ⁺¹⁹ ₋₅	4.4
J0519+0007	0.08875 ^{+0.00461} _{-0.00402}	675 ⁺¹⁴³ ₋₁₁₀	0.34 ^{+0.27} _{-0.26}	3.35 ^{+0.64} _{-0.59}	16,036. ^{+2738.} _{-2732.}	0.16 ^{+0.04} _{-0.04}	0.00 ^{+0.72} _{-0.00}	235 ⁺¹⁵³² ₋₂₃₅	4.3
SBS 0940+544 2	0.08179 ^{+0.00252} _{-0.00316}	77 ⁺²¹ ₋₁₇	0.42 ^{+0.14} _{-0.16}	0.00 ^{+0.28} _{-0.00}	18,232. ^{+1324.} _{-1629.}	0.06 ^{+0.02} _{-0.02}	2.62 ^{+1.02} _{-1.14}	6 ⁺¹¹ ₋₆	1.6
Tol 65	0.07883 ^{+0.00195} _{-0.00294}	244 ⁺⁶⁹ ₋₂₉	0.66 ^{+0.08} _{-0.09}	0.00 ^{+0.49} _{-0.00}	18,403. ^{+1124.} _{-2556.}	0.10 ^{+0.02} _{-0.02}	4.70 ^{+0.76} _{-1.03}	6 ⁺¹⁴ ₋₆	4.1
SBS 1415+437 (No. 1) 3	0.07694 ^{+0.00494} _{-0.00396}	136 ⁺⁸⁰ ₋₄₅	0.27 ^{+0.12} _{-0.13}	1.10 ^{+0.76} _{-0.74}	14,621. ^{+2817.} _{-2602.}	0.11 ^{+0.03} _{-0.03}	0.82 ^{+1.18} _{-0.82}	56 ⁺²⁶⁹ ₋₅₆	2.7
SBS 1415+437 (No. 2)	0.08226 ^{+0.00341} _{-0.00343}	87 ⁺⁴⁹ ₋₂₈	0.48 ^{+0.09} _{-0.09}	0.98 ^{+0.65} _{-0.63}	15,531. ^{+2056.} _{-2122.}	0.00 ^{+0.01} _{-0.00}	3.54 ^{+0.63} _{-0.71}	0 ⁺⁴¹ ₋₀	1.4
CGCG 007-025 (No. 2)	0.08867 ^{+0.00462} _{-0.00623}	181 ⁺¹⁰³ ₋₃₆	0.33 ^{+0.20} _{-0.20}	0.46 ^{+1.02} _{-0.46}	16,444. ^{+2449.} _{-3685.}	0.11 ^{+0.04} _{-0.04}	3.01 ^{+1.64} _{-2.20}	126 ⁺¹³⁰³ ₋₁₂₆	1.8
Mrk 209	0.08114 ^{+0.00272} _{-0.00186}	86 ⁺²⁷ ₋₂₁	0.29 ^{+0.08} _{-0.08}	0.24 ^{+0.40} _{-0.24}	16,207. ^{+1862.} _{-1619.}	0.00 ^{+0.02} _{-0.00}	2.59 ^{+0.85} _{-0.82}	0 ⁺¹⁹ ₋₀	0.3
SBS 1030+583	0.07937 ^{+0.00306} _{-0.00255}	47 ⁺²⁸ ₋₁₈	0.22 ^{+0.07} _{-0.08}	0.31 ^{+0.50} _{-0.31}	15,114. ^{+1736.} _{-1820.}	0.00 ^{+0.02} _{-0.00}	1.40 ^{+0.35} _{-0.39}	0 ⁺⁴⁹ ₋₀	1.6
Mrk 71 (No. 1)	0.08539 ^{+0.00374} _{-0.00445}	150 ⁺⁶⁴ ₋₃₃	0.49 ^{+0.11} _{-0.13}	1.25 ^{+0.71} _{-0.55}	15,724. ^{+2245.} _{-2469.}	0.08 ^{+0.02} _{-0.02}	3.87 ^{+2.22} _{-2.38}	59 ⁺²¹⁴ ₋₅₉	2.5
SBS 1152+579	0.08139 ^{+0.00272} _{-0.00303}	452 ⁺¹⁹⁷ ₋₁₀₆	0.30 ^{+0.08} _{-0.07}	0.93 ^{+0.59} _{-0.50}	16,090. ^{+2547.} _{-3060.}	0.17 ^{+0.03} _{-0.02}	4.26 ^{+1.16} _{-1.34}	100 ⁺⁶²² ₋₁₀₀	1.5
Mrk 59	0.08548 ^{+0.00405} _{-0.00177}	22 ⁺¹³ ₋₁₃	0.52 ^{+0.07} _{-0.05}	0.73 ^{+0.34} _{-0.44}	14,558. ^{+1817.} _{-1158.}	0.12 ^{+0.02} _{-0.02}	1.72 ^{+0.77} _{-0.44}	0 ⁺⁶² ₋₀	0.7
SBS 1135+581	0.08462 ^{+0.00072} _{-0.00063}	1 ⁺³ ₋₁	0.39 ^{+0.04} _{-0.04}	1.18 ^{+0.29} _{-0.32}	11,226. ^{+553.} _{-508.}	0.11 ^{+0.02} _{-0.02}	2.89 ^{+0.28} _{-0.24}	0 ⁺⁴⁷² ₋₀	4.9
Mrk 450 (No. 1)	0.08634 ^{+0.00441} _{-0.00335}	97 ⁺⁴² ₋₂₈	0.37 ^{+0.20} _{-0.20}	2.27 ^{+0.53} _{-0.48}	12,979. ^{+1321.} _{-1476.}	0.15 ^{+0.03} _{-0.03}	2.31 ^{+1.62} _{-1.65}	171 ⁺⁶⁰¹ ₋₁₇₁	5.5
Final Dataset with Flags									
SBS 0335-052E2	0.08007 ^{+0.00407} _{-0.00301}	136 ⁺⁵² ₋₃₅	0.47 ^{+0.08} _{-0.08}	4.28 ^{+0.68} _{-0.72}	19,971. ^{+3345.} _{-2984.}	0.04 ^{+0.02} _{-0.02}	3.11 ^{+1.18} _{-0.99}	2 ⁺⁵ ₋₂	3.9
Mrk 1315	0.09341 ^{+0.00274} _{-0.00184}	10 ⁺¹¹ ₋₁₀	0.32 ^{+0.15} _{-0.15}	0.81 ^{+0.38} _{-0.43}	11,653. ^{+1218.} _{-1024.}	0.11 ^{+0.02} _{-0.02}	0.00 ^{+1.04} _{-0.00}	3058 ⁺⁷¹⁰¹ ₋₂₂₇₆	4.5
Mrk 1329	0.09060 ^{+0.00425} _{-0.00204}	101 ⁺³⁴ ₋₃₄	0.25 ^{+0.15} _{-0.11}	1.03 ^{+0.42} _{-0.44}	11,223. ^{+1457.} _{-1006.}	0.17 ^{+0.02} _{-0.03}	0.11 ^{+1.56} _{-0.11}	1613 ⁺⁵⁴³⁵ ₋₁₄₇₃	5.0

Table 3. Physical parameters and He⁺/H⁺ abundance solutions of the Final Dataset

6 Results from the Final Dataset

Following the results of the previous sections, we now calculate the primordial helium abundance (mass fraction), Y_p , from the data listed in table 3. A regression of Y , the helium mass fraction, versus O/H , the oxygen to hydrogen mass fraction, is used to extrapolate to the primordial value¹. The O/H values are taken directly from ITS07[37].

The relevant values for the Final Dataset’s regression are given in table 4. The regression based on the 15 qualifying objects yields,

$$Y_p = 0.2449 \pm 0.0040, \quad (6.1)$$

with a slope of 79 ± 43 and a total χ^2 of 7.6. The result is shown in figure 6 and summarized in table 5. This result for Y_p agrees well with the SBBN value of $Y_p = 0.2471 \pm 0.0002$ [22], based on the Planck determined baryon density [4]. Not surprisingly, eq. (6.1) also agrees well with the SBBN-independent, direct Planck estimation of $Y_p = 0.251 \pm 0.027$. AOPS determined $Y_p = 0.2465 \pm 0.0097$ with a slope of 96 ± 122 . The result from AOPS is in good agreement with the newer result. Restricting the qualifying AOPS dataset to the 11 objects which are shared with the qualifying dataset of this work, results in $Y_p = 0.2461 \pm 0.0107$ with slope 84 ± 144 , again in good agreement with this result found in eq. (6.1). Due to five more objects qualifying, the Final Dataset of this work contains a similar number of objects as in AOPS (16 there, 15 here). However, as a result of the reduction in the individual y^+ uncertainties (see §5), the uncertainty on the intercept and slope are each reduced by approximately 60%. The intercept value decreased by 0.65% compared to AOPS. Given that the uncertainty on the intercept determination in AOPS was 3.9%, this decrease is not significant.

Including the 3 flagged objects² decreases the intercept and reduces the uncertainty to 0.2424 ± 0.0034 with a slope of 116 ± 32 . The reduced uncertainty is primarily a result of the increased number of points in the regression, while the decreased intercept is *entirely* the result of the increased slope. As was seen in AOS3 & AOPS, the flagged data points tend to have higher helium abundances, primarily due to the objects flagged for large neutral hydrogen fractions. In previous analyses, where the evidence for a non-zero slope was marginal, we have reported the mean value of Y . The mean value of Y for the Final Dataset using only qualifying points is $\langle Y \rangle = 0.2515 \pm 0.0017$. The mean value *increases* to $\langle Y \rangle = 0.2533 \pm 0.0016$, when the flagged objects are included. Olive & Skillman [27] restricted the metallicity baseline to $O/H \leq 9.2 \times 10^{-5}$. Adopting the same metallicity cut with the dataset of this work increases the intercept to 0.2466 ± 0.0063 , in near perfect agreement with the SBBN result using the Planck baryon density. Note, however, that in this case the reduced baseline leaves us with an undetermined slope, and for this case alone, basing the primordial abundance on the mean value given in the table 5 is justified.

Instead, if a regression analysis is performed excluding the T(O III) prior, the 12 qualifying objects yield $Y_p = 0.2379 \pm 0.0050$. However, the loss of the information provided by the T(O III) prior and the reduced sample size weakens the value of this determination. Nevertheless, the substantial reduction in the value of the intercept raises some questions regarding possible systematic errors when the prior is dropped.

¹This work takes $Z = 20(O/H)$ such that $Y = \frac{4y(1-20(O/H))}{1+4y}$

²One of the flagged objects is another independent observation of SBS 0335-052E that is combined with its two qualifying observations.

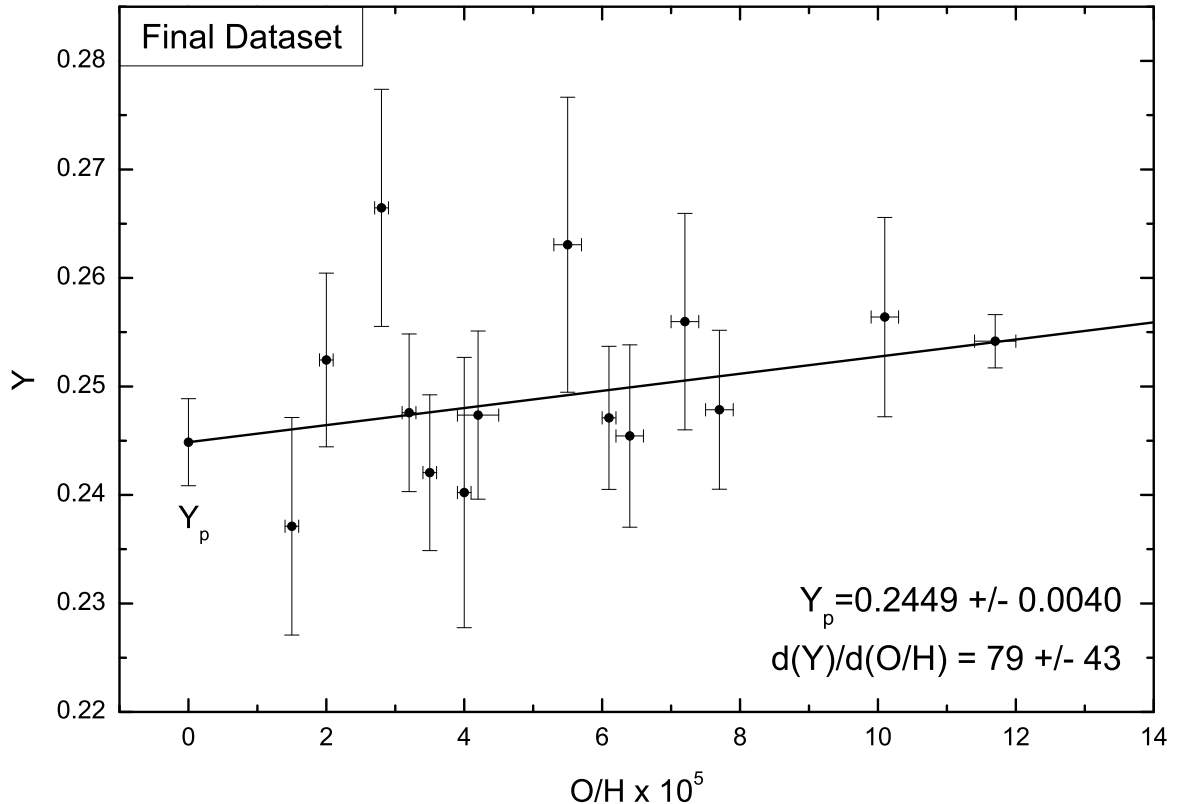


Figure 6. Helium abundance (mass fraction) versus oxygen to hydrogen ratio regression calculating the primordial helium abundance.

Starting with the 75 observations corresponding to the 45 H II regions for which they observed near-infrared spectra to measure He I $\lambda 10830$, ITG14 select 28 for which $W(H\beta) \geq 150$ Å, $O^{++}/O \geq 0.8$, and $\sigma(Y)/Y \leq 3\%$. Their resulting regression analysis and accounting of the dominant systematic uncertainties finds $Y_p = 0.2551 \pm 0.0022$. The significant differences between their result and the result derived here are due both to differences in determining the helium abundances for individual objects and in how the samples are defined.

7 Discussion

The primary aim of this work was to evaluate the effects of adding He I $\lambda 10830$ to a helium abundance analysis based solely on optical emission lines. In particular, it was hoped that this emission line, due to its much stronger electron density dependence, would have a significant effect in constraining the density in our solutions and, thereby, effectively break the degeneracy between temperature and density. Preliminary synthetic testing and analysis of H II region observations showed the positive impact of He I $\lambda 10830$ in improving the determination of our solution parameters, n_e , T_e , and of primary interest, y^+ . Most objects saw their y^+ uncertainty decrease by $\sim 50\%$, with a corresponding, similar improvement in the precision of Y_p .

Our determination of $Y_p = 0.2449 \pm 0.0040$ is in good agreement with the SBBN predicted value (as well as our previous results), and while the value of the intercept has decreased, it differs from the SBBN prediction by approximately $1/2 \sigma$, even with its most wel-

Object	He ⁺ /H ⁺	He ⁺⁺ /H ⁺	Y	O/H × 10 ⁵
Final Dataset Not Flagged (Qualifying)				
I Zw 18 SE 1	0.07693 ± 0.00423	0.0008 ± 0.0008	0.2371 ± 0.0100	1.5 ± 0.1
SBS 0335-052E1+3 ^(a)	0.08201 ± 0.00303	0.0026 ± 0.0018	0.2524 ± 0.0080	2 ± 0.1
J0519+0007	0.08875 ± 0.00461	0.0021 ± 0.0021	0.2665 ± 0.0109	2.8 ± 0.1
SBS 0940+544 2	0.08179 ± 0.00316	0.0005 ± 0.0005	0.2476 ± 0.0073	3.2 ± 0.1
Tol 65	0.07883 ± 0.00294	0.0011 ± 0.0011	0.2421 ± 0.0072	3.5 ± 0.1
SBS 1415+437 (No. 1) 3	0.07694 ± 0.00494	0.0022 ± 0.0022	0.2402 ± 0.0125	4 ± 0.1
SBS 1415+437 (No. 2)	0.08226 ± 0.00343	0.0000 ± 0.0000	0.2474 ± 0.0078	4.2 ± 0.3
CGCG 007-025 (No. 2)	0.08867 ± 0.00623	0.0007 ± 0.0007	0.2631 ± 0.0136	5.5 ± 0.2
Mrk 209	0.08114 ± 0.00272	0.0011 ± 0.0011	0.2471 ± 0.0066	6.1 ± 0.1
SBS 1030+583	0.07937 ± 0.00306	0.0021 ± 0.0021	0.2454 ± 0.0084	6.4 ± 0.2
Mrk 71 (No. 1)	0.08539 ± 0.00445	0.0008 ± 0.0008	0.2560 ± 0.0100	7.2 ± 0.2
SBS 1152+579	0.08139 ± 0.00303	0.0012 ± 0.0012	0.2478 ± 0.0073	7.7 ± 0.2
Mrk 59	0.08548 ± 0.00405	0.0010 ± 0.0010	0.2564 ± 0.0092	10.1 ± 0.2
SBS 1135+581	0.08462 ± 0.00072	0.0008 ± 0.0008	0.2542 ± 0.0025	11.7 ± 0.3
Mrk 450 (No. 1)	0.08634 ± 0.00441	0.0003 ± 0.0003	0.2565 ± 0.0097	15.2 ± 0.4
Final Dataset with Flags				
SBS 0335-052E1+2+3 ^(a)	0.08132 ± 0.00243	0.0025 ± 0.0015	0.2509 ± 0.0064	2 ± 0.1
Mrk 1315	0.09341 ± 0.00274	0.0000 ± 0.0000	0.2710 ± 0.0058	18.9 ± 0.4
Mrk 1329	0.09060 ± 0.00425	0.0000 ± 0.0000	0.2650 ± 0.0091	19.2 ± 0.5

^(a) SBS 0335-052E1, SBS 0335-052E2, & SBS 0335-052E3 are independent observations of the same H II region. As such, they were combined by weighted average into a single regression point.

Table 4. Primordial helium regression values

Dataset	N	Y _p	dY/d(O/H)	<Y>
Qualifying	15	0.2449 ± 0.0040	79 ± 43	0.2515 ± 0.0017
Qualifying + Flagged	17	0.2424 ± 0.0034	116 ± 32	0.2533 ± 0.0016
Qualifying ^(a) , O/H < 9.2 × 10 ⁻⁵	12	0.2466 ± 0.0063	35 ± 125	0.2482 ± 0.0025
Qualifying, T(O III) prior removed	12	0.2379 ± 0.0050	145 ± 52	0.2508 ± 0.0019

^(a) Olive & Skillman [27] restricted the metallicity baseline to O/H ≤ 9.2 × 10⁻⁵, and the same dataset was analyzed in AOS & AOS2 [29, 39].

Table 5. Comparison of Y_p for selected datasets

come increased precision. There are, however, potential systematic effects to be addressed. First, the inclusion of the near-infrared He I λ10830 with existing optical spectra requires scaling of He I λ10830 (see §4). This naturally raises the possibility of introducing additional error or systematic bias. Second, as discussed in Porter et al. [44] and updated in Porter, Ferland, Storey, & Detisch [32], the helium emissivities, the primary driver in determining the helium abundance from the observed fluxes, carry estimated uncertainties of ~0.2-0.7%. Furthermore, significant, systematic improvements in the helium emissivities have been made in recent years [32, 45]. Any further shifts in these emissivities will have a significant effect on the determination of Y_p.

The impressive benefits from including He I λ10830 in nebular helium abundance determinations strongly supports the case for additional near-infrared spectral observations of low-metallicity H II regions. In particular, to remove potential systematic effects introduced by scaling He I λ10830 observations, simultaneous observations of the optical and infrared

spectra would be decisive. Coupled with the opportunity for higher quality, higher resolution spectra, collection of simultaneous optical and infrared spectra would be of considerable value and utility. In sum, there is potential to significantly reduce the uncertainty in the determination of Y_p .

Acknowledgments

We would like to thank Sergio Sımon-Dıaz, Max Pettini, and Ryan Cooke for valuable conversations. This work has made use of NASA’s Astrophysics Data System Bibliographic Services and the NASA/IPAC Extragalactic Database (NED), which is operated by the Jet Propulsion Laboratory, California Institute of Technology, under contract with the National Aeronautics and Space Administration.

The work of KAO is supported in part by DOE grant DE-SC0011842. EDS is grateful for partial support from the University of Minnesota.

References

- [1] G. Hinshaw *et al.* [WMAP Collaboration], *Astrophys. J. Suppl.* **208** (2013) 19 [arXiv:1212.5226 [astro-ph.CO]];
- [2] E. Komatsu *et al.* [WMAP Science Team Collaboration], *PTEP* **2014**, no. 6, 06B102 (2014) [arXiv:1404.5415 [astro-ph.CO]].
- [3] P. A. R. Ade *et al.* [Planck Collaboration], *Astron. Astrophys.* **571**, A16 (2014) [arXiv:1303.5076 [astro-ph.CO]].
- [4] P. A. R. Ade *et al.* [Planck Collaboration], arXiv:1502.01589 [astro-ph.CO].
- [5] T. P. Walker, G. Steigman, D. N. Schramm, K. A. Olive and H. S. Kang, *Astrophys. J.* **376**, 51 (1991).
- [6] K. A. Olive, G. Steigman and T. P. Walker, *Phys. Rept.* **333**, 389 (2000) [arXiv:astro-ph/9905320].
- [7] B. D. Fields and S. Sarkar, in K. A. Olive *et al.* [Particle Data Group Collaboration], *Chin. Phys. C* **38**, 090001 (2014).
- [8] R. H. Cyburt, B. D. Fields and K. A. Olive, *Astropart. Phys.* **17**, 87 (2002) [astro-ph/0105397].
- [9] R. H. Cyburt, B. D. Fields and K. A. Olive, *New Astron.* **6**, 215 (2001) [arXiv:astro-ph/0102179].
- [10] A. Coc, E. Vangioni-Flam, M. Casse and M. Rabiet, *Phys. Rev. D* **65**, 043510 (2002) [arXiv:astro-ph/0111077].
- [11] R. H. Cyburt, B. D. Fields and K. A. Olive, *Phys. Lett. B* **567**, 227 (2003) [astro-ph/0302431].
- [12] A. Coc, E. Vangioni-Flam, P. Descouvemont, A. Adahchour and C. Angulo, *Astrophys. J.* **600**, 544 (2004) [arXiv:astro-ph/0309480].
- [13] R. H. Cyburt, *Phys. Rev. D* **70**, 023505 (2004) [arXiv:astro-ph/0401091].
- [14] P. Descouvemont, A. Adahchour, C. Angulo, A. Coc and E. Vangioni-Flam, *Atomic Data and Nuclear Data Tables*, **88**, 203 (2004) [arXiv:astro-ph/0407101].
- [15] A. Cuoco, F. Iocco, G. Mangano, G. Miele, O. Pisanti and P. D. Serpico, *Int. J. Mod. Phys. A* **19**, 4431 (2004) [arXiv:astro-ph/0307213].
- [16] P. D. Serpico, S. Esposito, F. Iocco, G. Mangano, G. Miele and O. Pisanti, *JCAP* **0412**, 010 (2004) [arXiv:astro-ph/0408076].

- [17] R. H. Cyburt, B. D. Fields and K. A. Olive, JCAP **0811**, 012 (2008) [arXiv:0808.2818 [astro-ph]].
- [18] O. Pisanti, A. Cirillo, S. Esposito, F. Iocco, G. Mangano, G. Miele and P. D. Serpico, Comput. Phys. Commun. **178**, 956 (2008) [arXiv:0705.0290 [astro-ph]].
- [19] A. Coc, S. Goriely, Y. Xu, M. Saimpert and E. Vangioni, arXiv:1107.1117 [astro-ph.CO].
- [20] A. Coc, J. -P. Uzan and E. Vangioni, arXiv:1307.6955 [astro-ph.CO].
- [21] A. Coc, J. P. Uzan and E. Vangioni, JCAP **1410** (2014) 050 [arXiv:1403.6694 [astro-ph.CO]].
- [22] R. H. Cyburt, B. D. Fields, K. A. Olive, and T.-H. Yeh, in preparation, 2015.
- [23] R. Cooke, M. Pettini, R. A. Jorgenson, M. T. Murphy and C. C. Steidel, Ap. J. **781**, 31 (2014) [arXiv:1308.3240 [astro-ph.CO]].
- [24] K. A. Olive *et al.* [Particle Data Group Collaboration], Chin. Phys. C **38**, 090001 (2014).
- [25] R. H. Cyburt, B. D. Fields, K. A. Olive and E. Skillman, Astropart. Phys. **23**, 313 (2005) [arXiv:astro-ph/0408033].
- [26] K. A. Olive and E. D. Skillman, New Astron. **6**, 119 (2001) arXiv:astro-ph/0007081.
- [27] K. A. Olive and E. D. Skillman, Astrophys. J. **617**, 29 (2004) [arXiv:astro-ph/0405588].
- [28] M. Peimbert and S. Torres-Peimbert, Astrophys. J. **193**, 327 (1974)
- [29] E. Aver, K. A. Olive and E. D. Skillman, JCAP **1103**, 043 (2011) [arXiv:1012.2385 [astro-ph.CO]] (AOS2).
- [30] E. Aver, K. A. Olive and E. D. Skillman, JCAP **1204**, 004 (2012) [arXiv:1112.3713 [astro-ph.CO]] (AOS3).
- [31] E. Aver, K. A. Olive, R. L. Porter and E. D. Skillman, JCAP **1311**, 017 (2013) [arXiv:1309.0047 [astro-ph.CO]].
- [32] R. L. Porter, G. J. Ferland, P. J. Storey and M. J. Detisch, Mon. Not. Roy. Astron. Soc. **425**, L28 (2012) arXiv:1206.4115 [astro-ph.CO] (PFSD).
- [33] R. L. Porter, G. J. Ferland, P. J. Storey and M. J. Detisch, Mon. Not. Roy. Astron. Soc. **433**, L89 (2013) arXiv:1303.5115 [astro-ph.CO].
- [34] A. Peimbert, M. Peimbert and V. Luridiana, Astrophys. J. **565**, 668 (2002) arXiv:astro-ph/0107189.
- [35] N. G. Guseva, Y. Izotov and T. X. Thuan, Astrophys. J. **644**, 890 (2006) [arXiv:astro-ph/0603134].
- [36] N. G. Guseva, Y. I. Izotov, P. Papaderos and K. J. Fricke, arXiv:astro-ph/0701032.
- [37] Y. I. Izotov, T. X. Thuan and G. Stasińska, Astrophys. J. **662**, 15 (2007) [arXiv:astro-ph/0702072] (ITS07).
- [38] Y. I. Izotov, T. X. Thuan and N. G. Guseva, Mon. Not. Roy. Astron. Soc. **445**, 778 (2014) [arXiv:1408.6953 [astro-ph.CO]]. (ITG14)
- [39] E. Aver, K. A. Olive and E. D. Skillman, JCAP **1005**, 003 (2010) [arXiv:1001.5218 [astro-ph.CO]] (AOS).
- [40] R. A. Benjamin, E. D. Skillman and D. P. Smits, Astrophys. J. **569**, 288 (2002) [astro-ph/0202227].
- [41] P. S. Conti & I. D. Howarth, Mon. Not. Roy. Astron. Soc. **302**, 145 (1999).
- [42] D. G. Hummer and P. J. Storey, Mon. Not. Roy. Astron. Soc. **224**, 801 (1987).
- [43] H. Anderson, C. P. Ballance, N. R. Badnell and H. P. Summers, J. Phys. B: At. Mol. Opt.

Phys. **35**, 1613 (2002).

[44] R. L. Porter, G. J. Ferland, K. B. MacAdam and P. J. Storey, Mon. Not. Roy. Astron. Soc. **393**, 36 (2009) [arXiv:0811.1216 [astro-ph]].

[45] R. L. Porter, G. J. Ferland and K. B. MacAdam, Astrophys. J. **657**, 327 (2007) [arXiv:astro-ph/0611579] (PFM).